Advanced Electronic Materials 8.2 (2022): 2100761

DOI: https://doi.org/10.1002/aelm.202100761

Light and Thermally-Induced Charge Transfer and Ejection of Micro/Nanoparticles from Ferroelectric Crystal Surfaces

*Carlos Sebastián-Vicente, Angel García-Cabañes, Fernando Agulló-López, and Mercedes Carrascosa**

C. Sebastián-Vicente, Dr. A. García-Cabañes, Prof. F. Agulló-López, Prof. M. Carrascosa
Departamento de Física de Materiales, Universidad Autónoma de Madrid, c/ Francisco Tomás y Valiente 7, 28049 Madrid, Spain
E-mail: m.carrascosa@uam.es

Dr. A. García-Cabañes, Prof. F. Agulló-López, Prof. M. Carrascosa
Instituto de Ciencia de Materiales Nicolás Cabrera, Universidad Autónoma de Madrid, 28049 Madrid, Spain

Keywords: ferroelectric platforms, bulk photovoltaic effect, pyroelectric effect, charge transfer, nanoparticles, ferroelectric crystals

Abstract

During real-time operation of photovoltaic optoelectronic tweezers a novel intriguing phenomenon has been recently observed, namely, silver nanoparticles previously deposited on ferroelectric $LiNbO_3$:Fe surfaces were ejected from them by illumination. In this work, it is shown that this phenomenon results from the electrical charging of the micro/nanoparticles previously trapped on the $LiNbO_3$:Fe surfaces and the subsequent Coulomb repulsion. Specific experiments are performed to determine the sign of the transferred charges, which is negative/positive for the $+c/-c$ sample face, i.e. it coincides with that of the stored charges on each surface. The charging/ejection process is proved to occur regardless of the illuminated crystal surface, the dielectric or metallic nature of the particles, and in different surrounding media. Besides, the role of the excitation light intensity is also explored. Next, to assess the generality of the ejection phenomenon, similar experiments based on the pyroelectric effect are performed, i.e. generating the electric fields by changing the crystal temperature instead of illuminating it. Thereby, thermally-driven particle ejection is demonstrated using different ferroelectric crystals. The similarities found for the two approaches throw light on the charge

transfer and ejection mechanism and remark the universality of the phenomenon for ferroelectrics, which can find many technological applications.

1. Introduction

Ferroelectric materials are becoming efficient platforms for a broad variety of applications in bio- and nano-technology.[1–8] In particular, a great potential has been shown for electric-field-assisted manipulation and trapping of micro/nanoparticles and biomaterials.[1,9–14] The electric fields can be induced by different physical stimuli, such as visible light illumination via the bulk photovoltaic (PV) effect or temperature changes via the pyroelectric (PY) effect, allowing handling and trapping particles being close to the ferroelectric platform. Numerous works have been reported on these techniques and their multiple applications. Some reviews or reference works are refs. [12,15,16] for photovoltaic optoelectronic tweezers (PVOT), and refs. [10,17,18] for PY trapping.

The particle ejection phenomenon reported in this paper has been incidentally discovered during particle manipulation with PVOT.[19] The so-called PVOT are a rather recent technique that has undergone a rapid development in the last few years,[16] based on the electric fields generated by the bulk PV effect. This effect is a singular phenomenon which strongly appears in a few crystalline ferroelectric materials,[20,21] such as $LiNbO_3$ (LN), when properly doped (mainly Fe or Cu). It allows the generation of remarkably high electric fields (up to ~1.5×10^5 V/cm)[22] for moderate or low light excitation levels (~mW/cm^2). The PV effect is associated with optical transitions from localized states of impurities, such as Fe^{2+}/Fe^{3+} or Cu^{+}/Cu^{2+}, and with a directional electron migration along the polar axis (PV current). Once displaced, the electrons are trapped in other defects and generate a spatial charge distribution and the corresponding electric field,[23] which are illustrated in **Figure 1**. Two crystal configurations (parallel and perpendicular), commonly used for particle manipulation, are shown.[24,25] They are defined by

the orientation of the polar axis, parallel or perpendicular to the active surface, respectively. The PV electric field extends near the surface outside the crystal (evanescent PV fields), where it can act either on charged particles via electrophoretic forces, or on neutral objects polarized by the field via dielectrophoretic forces,[26,27] as illustrated in Figure 1.

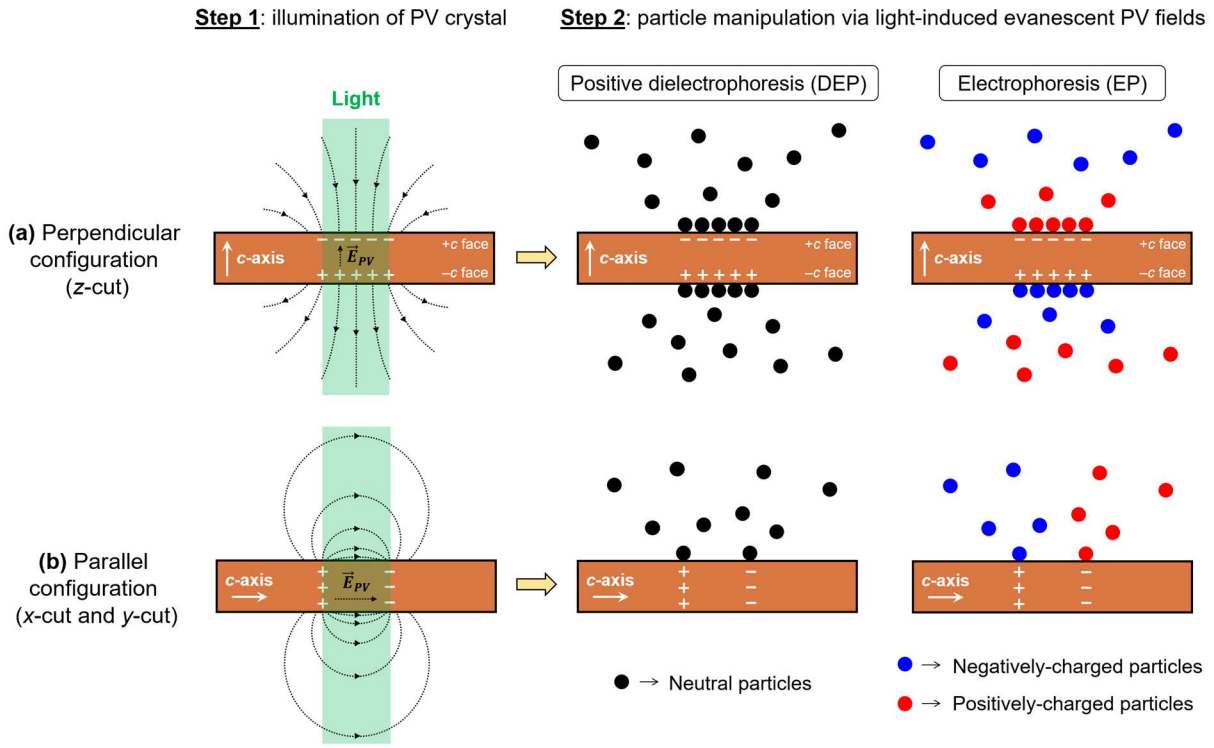

Figure 1. Illustration of the typical steps involved in particle manipulation via PV electric fields, which may be carried out sequentially or simultaneously. The PV space-charge distribution, electric field lines and specific features of the dielectrophoretic/electrophoretic manipulation process are depicted for the two available configurations of monodomain crystals: a) *z*-cut, and b) *x*-cut or *y*-cut, with the polar ferroelectric axis perpendicular or parallel to the substrate surface, respectively.

So far, the vast majority of the reported experimental results have been obtained by using a two-step sequential procedure: first, the PV substrate is illuminated, and then, the particles are manipulated and trapped by means of the light-induced PV electric fields. This sequential method can be employed because the PV fields remain after illumination for periods of time in the range of days to months unless they are thermally erased or externally screened. Although this method is quite convenient to trap particles and assemble permanent particle structures,

other applications require real-time manipulation. This issue was initially addressed in a recent paper,[19] where an alternative simultaneous procedure was explored: illumination of the PV crystal and particle manipulation are performed at the same time. Unexpectedly, when using the simultaneous method a novel feature of PVOT was observed, which consists of an efficient Ag nanoparticle untrapping and ejection effect during illumination. The synergy between this new ejection phenomenon and the already known trapping effect has suggested novel capabilities of PVOT for real-time manipulation and pattern reconfiguration.

From a more general point of view, this ejection effect points to a novel interaction mechanism between the ferroelectric surface and the particles that has not been investigated so far. Hence, the objective of this paper is to investigate thoroughly this phenomenon, providing further experimental evidence and determining its scope and limits. To this end, we have performed experiments probing different particles, both metallic (Ag and Al) and dielectric (Al_2O_3 and $CaCO_3$), in different surrounding media (heptane, water and air) and for various crystal orientations (perpendicular and parallel configurations). The role of the excitation light intensity that triggers the particle ejection phenomenon has also been investigated. These additional experimental data have allowed us to shed new light on the physical mechanism behind particle ejection. We propose that illumination activates a charge transfer between the PV substrate and the particles on its surface. Particles should get charged with the same sign as the crystal surface, being then repelled by electrophoretic forces. While this is a plausible explanation for the ejection effect, up to now there was no direct experimental evidence for this charge transfer. In Section 3.1 we provide it through a specific charge test and explain all the experiments on light-induced particle ejection within the framework of this charging mechanism.

Finally, the generality of this charge transfer process between ferroelectrics and micro/nanoparticles is established by additional experiments showing that it can also be thermally induced through the PY effect, exhibited by all ferroelectrics. Specifically, PY

particle ejection in the dark is demonstrated for a variety of ferroelectric crystals, namely $LiNbO_3$:Fe (LN:Fe), undoped LN and $LiTaO_3$ (LT). Furthermore, the fundamental as well as technological implications of the charging and ejection phenomenon are briefly discussed.

2. Light-Induced Ejection of Particles from $LiNbO_3$:Fe Surfaces

First preliminary results on light-induced ejection of Ag nanoparticles from a PV crystal were presented in a previous publication, which was focused on real-time operation of PVOT.[19] **Figure 2** shows several experimental results that summarize the observed behavior. After deposition of a uniform background of Ag particles dispersed in heptane on a *z*-cut LN:Fe crystal, the PV substrate was excited by a focused Gaussian beam (see Experimental Section). As a result, particles were repelled and ejected from the illuminated area, generating empty circles by static beams (Figure 2a) or empty tracks by moving beams (Figure 2b and 2c). Remarkably, the same ejection phenomenon was observed on both polar faces (+*c* and −*c*) with analogous behavior.

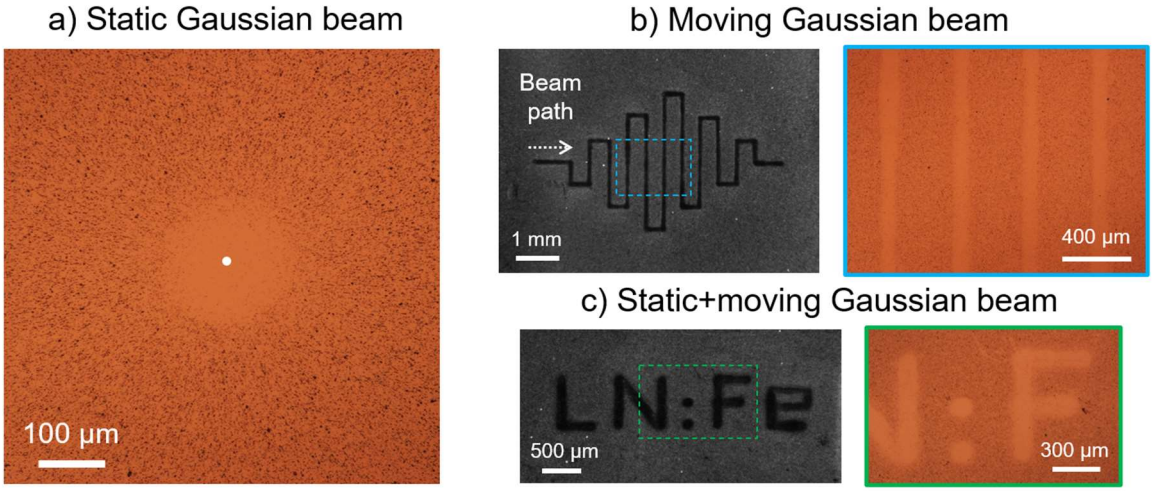

Figure 2. Representative results illustrating the effect of Ag nanoparticle ejection. a) Circle emptied of particles produced by illumination with a Gaussian beam (average intensity $I = 6.1$ W cm^{-2}, exposure time $\Delta t = 1$ min). The white dot indicates the center of the beam. b) Zigzag pattern generated by scanning the laser beam, which lifts off the particles along its path ($I = 6.1$ W cm^{-2}, average speed $v \approx 18$ µm/s). The figure includes a magnified inset of the central area. c) Acronym "LN:Fe" combining static and moving beams, together with a magnified inset of the central region ($I = 29$ W cm^{-2}, $v \approx 52$ µm/s, $\Delta t = 3$ s for each dot). All three experiments were conducted on the –*c* face of a *z*-cut crystal, the laser wavelength was $\lambda = 532$ nm and the $1/e^2$ spot size was $2w = 150$ µm.

In the next section, we report a broad set of novel data under different conditions and particles in order to offer a complete phenomenological framework and in-depth analysis of the ejection effect and its implications.

2.1. Dielectric vs Metallic Particles

In this work, the experiments have been extended to other metallic (Al) and dielectric (Al_2O_3 and $CaCO_3$) particles in order to compare their behaviors with that of metallic Ag particles (see **Figure 3**). In these experiments, an essentially uniform background of particles is first generated on the substrate by previous sedimentation in the dark. After that, the *z*-cut crystal is illuminated with a Gaussian beam (λ = 532 nm, $1/e^2$ spot diameter $2w$ = 150 μm) and the time evolution is registered. In the photographs of Figure 3a it is clearly observed that, when light is turned on, all kinds of particles (metallic and even dielectric) get progressively ejected from the light spot position. As a consequence, a particle-free circular area appears at the illuminated spot, and its radius monotonically increases with illumination time. In order to quantify this repulsive phenomenon, the diameters of the circles have been plotted in Figure 3b as a function of time for the four different types of particles and a fixed light intensity (6.1 W cm^{-2}). The kinetics and rates look quite similar in all cases, although the initial response of metallic particles was slightly faster. Therefore, all particles present similar behaviors, regardless of their metallic/dielectric character and their completely different crystallographic and electronic structure. These results imply that the effect is not restricted to a specific type of particle and we consider that they offer key elements when discussing possible physical mechanisms.

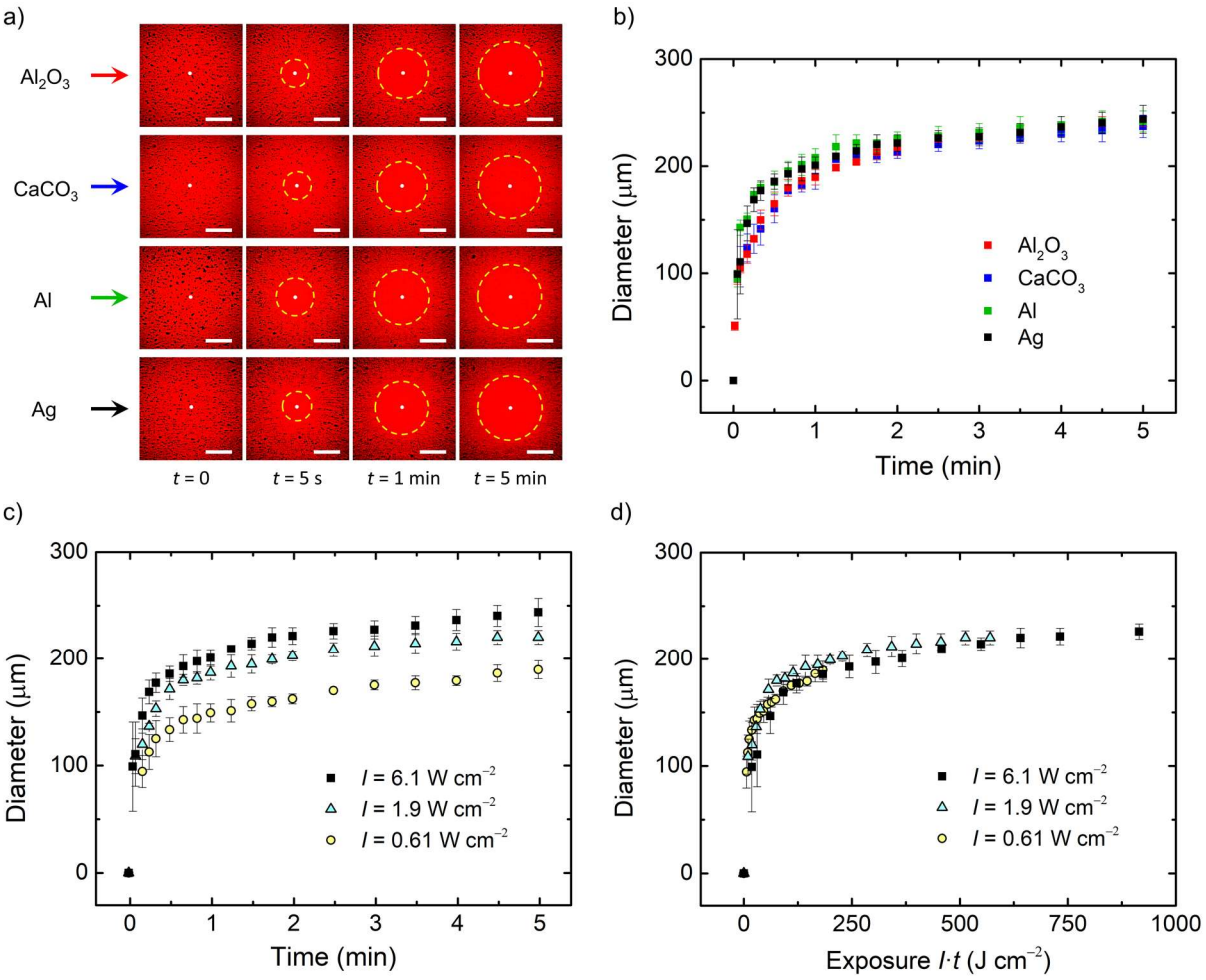

Figure 3. a) Temporal sequences of the particle distributions generated on a *z*-cut LN:Fe crystal (−*c* face) during illumination with a static Gaussian beam (λ = 532 nm, 2*w* = 150 µm, intensity *I* = 6.1 W cm^{-2}, position indicated by a white dot at the center). The crystal surface is initially covered by a uniform background of different particles, as shown at *t* = 0. Upon light excitation, particles are ejected away from the crystal surface giving rise to a circular area free of particles, enclosed by a dashed yellow line drawn as a guide for the eye. Scale bar: 100 µm. b) Time evolution of the diameters of the particle-free circular regions obtained in a). c) Time evolution of the circle diameters for several light intensities, using Ag particles in all cases. d) Diameters of graph c) plotted as a function of exposure (*I*·*t*).

2.2. Role of Light Intensity

Light intensity is another relevant parameter that has been investigated. The temporal dependence of the diameter of the empty circles is depicted in Figure 3c for three light intensities. The kinetics is analogous in all cases, although the evolution is clearly faster as the intensity increases. It is worthwhile noting that when the diameters are plotted as a function of

exposure instead of time, the obtained curves match quite well (see Figure 3d). This result suggests that the time evolution is governed, among other parameters, by the product $I \cdot t$, which is an important fact that must be taken into account when developing a model to explain the effect.

Although all the experiments of Figure 3 have been carried out on the $-c$ face of a *z*-cut crystal, additional experiments were conducted on the $+c$ face for comparison purposes. The first significant observation is that the ejection phenomenon occurs on both faces with all particles (metallic and dielectric). Moreover, the diameter of the curves for a given light intensity and a specific type of particles are similar and so, the effect and its kinetics seem to be essentially independent of the illuminated face.

2.3. *X*-cut vs *Z*-cut Substrates

To acquire a broader understanding of the effect, new results have also been obtained on *x*-cut samples, where the polar *c*-axis is parallel to the active surface instead of perpendicular to it (see Figure 1). The PV electric field distribution generated by such crystals for a given light pattern (a Gaussian beam in this case) is completely different from that of *z*-cut crystals. Interestingly, both positive and negative charges are present at different positions of the same face, as opposed to the polar faces of *z*-cut crystals. Consequently, *x*-cut substrates can offer valuable supplementary information concerning the ejection mechanism.

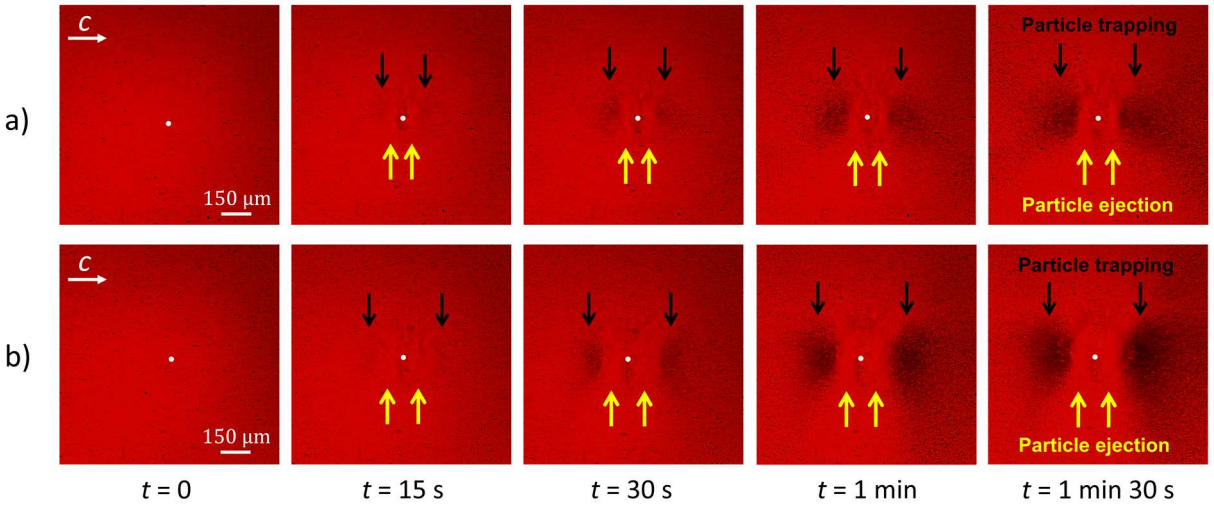

Figure 4. Temporal sequence of the Ag nanoparticle patterns obtained by the simultaneous method on an *x*-cut substrate for two light intensities of a) 3.4 W cm^{-2} and b) 6.1 W cm^{-2}. The position of the Gaussian beam is indicated by a white dot at the center. Owing to particle ejection, two narrow regions free of particles are obtained on both sides of the beam spot along the *c*-axis direction (similar to the empty circles that appear in *z*-cut substrates), highlighted by yellow arrows in the figure. At the same time, trapped particles accumulate in two different areas located further away from the center of the light spot along the *c*-axis, indicated by black arrows. The scale bar and direction of the *c*-axis are given in the images corresponding to $t = 0$.

The experimental procedure was analogous to that of Section 2.1 with *z*-cut crystals. As illustrated in the results of **Figure 4**, the effects in *x*-cut crystals are visibly different. First of all, the microphotographs show that a trapping pattern develops over time, similar to the one obtained with the sequential method and in good agreement with numerical simulations of the dielectrophoretic potential energy (see ref. [28]). More specifically, two trapping regions appear on both sides of the light spot along the *c*-axis direction. Nevertheless, there is one additional feature that stands out: two narrow regions free of particles are obtained on both sides of the beam spot along the *c*-axis direction, which for clarity have been indicated by yellow arrows in Figure 4. These empty regions, not reported before, resemble the empty circles obtained with *z*-cut crystals by particle ejection (see Figure 3). The fact that the shape, size and location of these particle-free regions are so different in *z*-cut and *x*-cut crystals is a clear evidence that the ejection effect has to do with the substrate, being correlated with the charge distribution and the PV field symmetry. Moreover, a comparison between Figure 4a and 4b shows that, the higher

the light intensity, the larger the trapping and the empty regions at a given instant due to a faster time evolution of the PV effect.[23]

On the other hand, although it was difficult to unequivocally keep track of individual particles during experiments, it was often possible to identify certain aggregates and follow them over time. By doing that, we have observed some of them jumping multiple times, back and forth, from one side of the light spot to the other along the *c*-axis direction (see Figure S1 in the Supporting Information). Such oscillations strongly suggest a successive reversal of the charge sign of the particles, which would be iteratively repelled from one side of the light spot and attracted by the other.

2.4. Experiments in Air

So far, all the successful experiments on particle ejection have been conducted with the substrate immersed in a nonpolar liquid, namely heptane. No ejection was observed when distilled or tap water was employed, very likely due to the efficient screening of the electric fields. In this section, we have performed analogous experiments in air, allowing us to easily track the trajectories of the ejected particles from the side. This configuration provides additional valuable information that cannot be inferred from Figure 3 and 4, where only a top view of the crystal surface is available. For this purpose, a lateral camera was added to the setup (see Experimental Section), with an exposure time per frame of 100 ms. With this acquisition time, long particle trajectories can be captured in a single frame. As for the experimental protocol, a simple procedure was followed: first, $CaCO_3$ particles were sprinkled onto the substrate surface to generate a uniform background, and then, it was illuminated with a Gaussian beam. It is worth noting that, unlike previous experiments, particle deposition is carried out directly from air (without dispersing the powder in a liquid by sonication). This leads to the presence of aggregates of various sizes that can be as large as around 1 mm, whose

motion can be straightforwardly traced. Moreover, here the laser was not focused, having a diameter of $2w$ = 3 mm and a low intensity of 86 mW cm^{-2}.

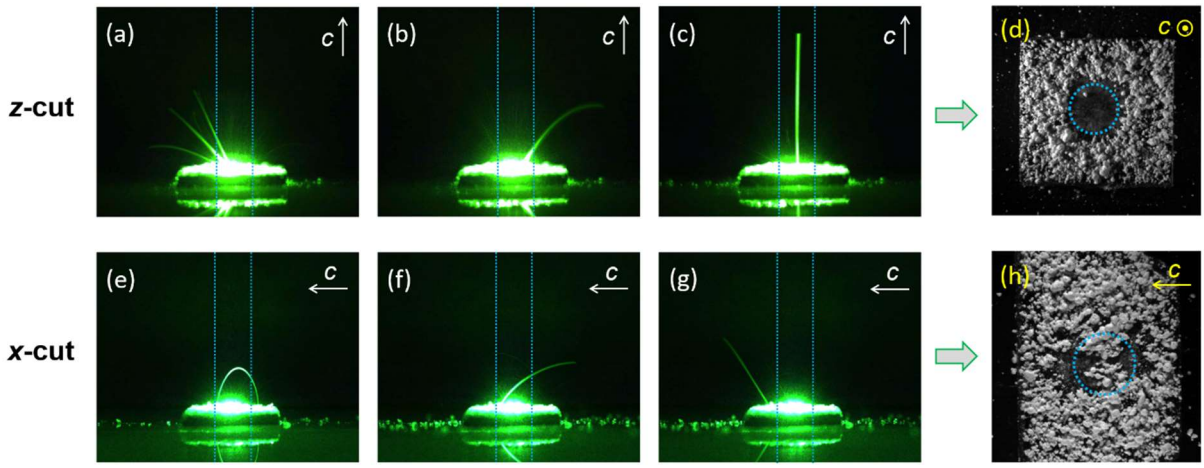

Figure 5. Images corresponding to two different ejection experiments conducted with air as surrounding medium. Top/bottom row: experiment with a *z*-cut/x-cut crystal. a)-c) and d)-g) are representative lateral images showing the trajectories of several particles being ejected from the surface of *z*-cut and *x*-cut crystals, respectively. d) and h) are top views of the surfaces after 10 min of light exposure, where regions free of particles can be clearly distinguished as a result of ejection. $CaCO_3$ particles were employed in both cases, and the blue dotted lines indicate the position and $2w$ diameter of the laser beam ($2w$ = 3 mm, I = 86 mW cm^{-2}, λ = 532 nm).

When light is switched on, particles start getting ejected away from the surface, which is the same effect that is observed in heptane. Initially there is a transitory stage (about a few seconds) where the ejection rate progressively increases due to the time required for the PV electric field to build up. Note that this time interval may be shortened/extended by suitably increasing/decreasing the beam intensity. If light excitation is maintained, we have observed that ejection continues as long as there are still particles remaining on the surface of the illuminated crystal area. Although both *z*-cut and *x*-cut crystals exhibit the ejection phenomenon (as expected based on the results of previous sections), their behaviors are quite different, as shown in **Figure 5** and Video S1 and S2 in the Supporting Information. In the case of *z*-cut crystals, particles are essentially ejected from the illuminated spot without any privileged direction. Their trajectories are increasingly tilted with respect to the normal of the surface as they are located further away from the center of the beam (see Figure 5a-c). In the limit case of

particles lying at the very center, they are ejected perpendicularly to the crystal surface (see Figure 5c). After 10 min of exposure, a circular area empty of particles is left behind (see Figure 5d), in good agreement with the results of Figure 3 in heptane. Although the experiment of Figure 5a-d corresponds to the +*c* face of the crystal, analogous experiments have been carried out on the −*c* face and no significant differences were found.

In contrast, particles on *x*-cut crystals are not repelled upon light excitation from the whole illuminated region, but only from two sub-areas (see Figure 5e-h). More specifically, only particles located on both sides of the beam along the *c*-axis direction are ejected. Three main types of trajectories can be distinguished. The most distinctive ones are closed arcs from side to side of the beam along the *c*-axis, as illustrated in Figure 5e. This kind of behavior is attributed to the presence of both positive and negative charges at *x*-cut surfaces: particles repelled from one side of the beam due to charge transfer are attracted by the other side, which has the opposite charge sign. Such arc-shaped trajectories, never observed with *z*-cut crystals, are very likely related to the "jumps" from side to side described in the previous section. The second type of trajectory corresponds to particles that, despite being ejected from one side to the other, cannot form a closed arc due to their inertia and end up outside the crystal (see Figure 5f). Finally, the particles that are located slightly further away from the center of the beam are ejected directly outwards (see Figure 5g). After 10 min of exposure, two empty regions are generated on both sides of the laser spot along a privileged direction that coincides with the polar *c*-axis. Again, these empty features are analogous to those of Figure 4 obtained in a heptane suspension. It must be emphasized that ejection does not occur at the central region of the laser spot, despite being illuminated. Also, no significant asymmetries were found between the +*c* and the −*c* sides.

One ~~final~~ more aspect worth discussing is that when light is suddenly switched off, there is a transient in which ejection activity persists before fully stopping. Therefore, the presence of

simultaneous optical excitation of charge carriers is not strictly necessary for the occurrence of ejection. A plausible explanation is that ejection continues in the dark until the electric field is screened to a point where ejection is no longer possible. In the framework of the charge transfer mechanism already invoked and discussed in more detail in the coming sections, the ejection phenomenon would be itself an additional screening mechanism of the PV charge at the ferroelectric surface, due to the charge transferred to the particles and carried away upon repulsion.

Finally, it is well known that the bulk PV effect of LN:Fe has a wide spectral response in the visible region ¿referencia?. Therefore, particle ejection is not restricted to the specific wavelength of 532 nm used throughout this work, but it exhibits a broadband excitation spectrum. Additional experiments have been conducted with a violet LED (center wavelength 390 nm, full width at half maximum 15 nm revisar) and a He-Ne laser (λ = 632.8 nm). We have verified that, indeed, ejection also occurs at these wavelengths, although it is notably slower/weaker at 632.8 nm due to a less efficient excitation of the bulk PV effect far from the absorption peak.

3. Charge Transfer between the Ferroelectric Crystal and Micro/Nanoparticles

In ref. [19], where preliminary data on the ejection phenomenon with Ag nanoparticles was reported, it was suggested that this effect might occur due to a charge transfer between the illuminated PV ferroelectric crystal and the particles. According to this proposal, particles get charged with the same sign as the corresponding polar face (negative at the +*c* face and positive at the −*c* face), leading to Coulomb repulsion and ejection (see **Figure 6**a). However, since this reasonable proposal has not been proved so far, we have designed and performed an experiment to check the charge state of the light-induced ejected particles.

3.1. Experimental Determination of the Charge Sign of the Ejected Particles

The charge test described next has been applied to particles ejected from *z*-cut LN:Fe crystals under illumination. It is based on a result reported in ref. [27], which takes advantage of an *x*-cut crystal as a charge sensor. The setup for this experiment is schematically shown in Figure 6b. Initially there are two crystals immersed in heptane. A *z*-cut crystal is placed vertically with one face in contact with a wall of a glass cuvette and the other face covered with a homogenous background of Ag particles. An *x*-cut crystal (charge sensor), which has been previously illuminated with a Gaussian beam at the position indicated by a blue dotted circle, is located at the bottom of the cuvette. In that situation, the *z*-cut crystal is illuminated ($2w$ = 3 mm, I = 0.29 W cm^{-2}, Δt = 2 min), and those particles that are ejected from its surface are subsequently trapped on the *x*-cut crystal. The image of Figure 6c shows the particle pattern obtained when the +*c* face of the *z*-cut crystal is illuminated, whereas Figure 6d shows the corresponding one when the −*c* face is illuminated. In Figure 6c particles only get trapped on the left side of the light spot (i.e. −*c* side) while, on the contrary, in Figure 6d particles only get rapped on the right side (i.e. +*c* side). This result demonstrates that particles get ejected with negative charge from the +*c* face and with positive charge from the −*c* face. Hence, the sign of the particle charge coincides with the sign of the PV charge stored at each polar surface of the PV substrate, thus explaining the repulsion behavior. Likewise, an analogous result has been achieved with dielectric $CaCO_3$ particles (see Figure S2). This new experimental finding provides essential information and, along with the rest of the evidence, confirms the proposed mechanism for particle ejection.

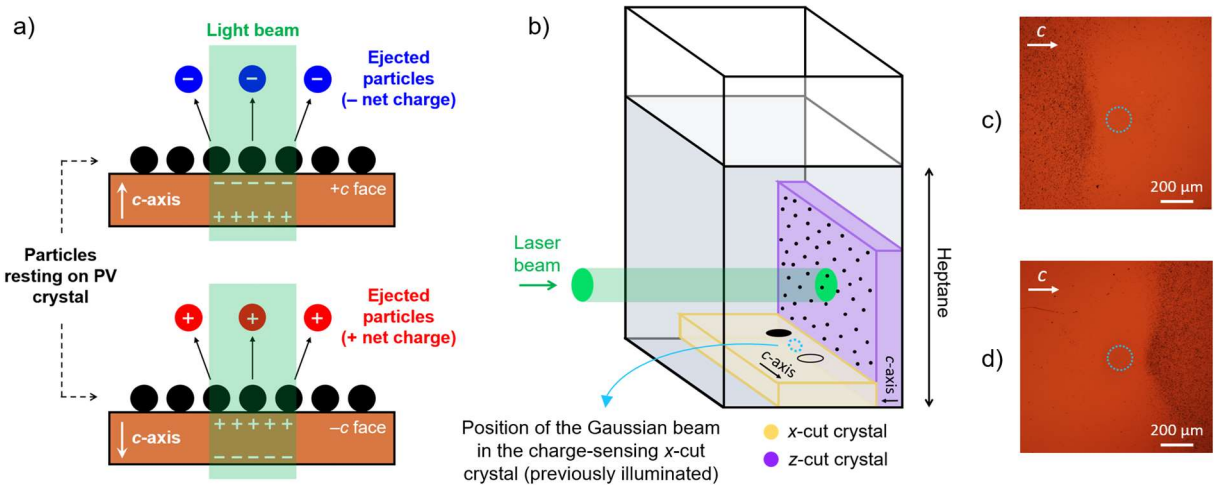

Figure 6. a) Schematics of the charge-transfer mechanism proposed to explain particle ejection from *z*-cut surfaces. b) Schematic view of the experimental configuration designed to test the charge-transfer mechanism (see text for a more detailed description). The results of c) and d) correspond to the trapping of Ag nanoparticles generated on the *x*-cut crystal during illumination of c) the $+c$ face and d) the $-c$ face of the *z*-cut crystal, respectively.

3.2. Discussion of Experimental Results on Light-Induced Particle Ejection

Let us now analyze the experimental results of Section 2 in the light of the charge transfer mechanism.

- The geometry and area of the empty regions due to particle ejection (see Figure 3, 4, 5d and 5h) coincide with the charged regions produced by the PV effect at the LN:Fe surface for both parallel and perpendicular configurations. Hence, they correspond to the regions with a dominant vertical component of the PV field. This can be qualitatively checked looking at the schematics of Figure 1 and, in more detail, from rigorous calculations for these charged regions generated under Gaussian illumination in *x*-cut[28] and *z*-cut[29] by the PV effect. In particular, in the case of *z*-cut the shape of the curve showing the diameter of the empty circle versus time (Figure 3b) is in good agreement with the simulations of the radius of the charged region reported in ref. [29].

- The sign of the particles coincides with that of the charge stored at the crystal surface from which they are ejected, as checked in Section 3.1 for *z*-cut. In the case of *x*-cut the sign is not

determined in the experiments but they show that the charge of the particles ejected from the two empty regions is opposite because particles are often ejected from one region and subsequently trapped at the other one. Hence, again the experimental evidence offered by the trajectories is in accordance with the charge transfer mechanism. Moreover, these trajectories are consistent with the symmetry of the electric fields of the two crystal configurations (see Figure 1). The particle charging process gives rise to a situation where electrophoretic forces dominate over dielectrophoretic forces. Thus, the path followed by the ejected particles is primarily determined by the spatial distribution of the PV electric field lines. Indeed, the different electric field distributions created by *z*-cut and *x*-cut crystals can very well account for the trajectories of Figure 5.

In summary, all the experimental results are consistent with a charge transfer process that ultimately triggers particle ejection. However, the physical mechanism underlying the charge transfer between the ferroelectric material and the particles is still open. It is well known that when electric fields are applied between electrodes (normally two parallel plates), different particle-electrode or even particle-particle charge transfer processes may take place.[30–35] In the simple case of a conductive particle in contact with one of the electrodes, a net charge is induced in the particle due to the flow of electrons from/to the electrode in search of electrostatic equilibrium (i.e. same electric potential). When the electric fields are sufficiently strong, particles acquire enough charge to lift off from the electrode surface due to Coulombian repulsion, somewhat resembling the ejection reported here. Likewise, electron transfer between two contacting conductive particles in an external field perpendicular to their interface readily occurs. However, when dielectric materials are involved, this mechanism is expected to be hindered by the availability of transferable electrons and/or suitable electronic states, and there is an ongoing discussion in the literature about the dominant mechanism in this situation.[36,37]

The complexity of this issue is aggravated in our case, where the PV ferroelectric substrate is an insulator in the dark whose photoconductivity increases with light intensity.

As an alternative, ion transfer enabled by the presence of tiny amounts of water adsorbed at the contacting surfaces (coming from ambient humidity)[38] has already been proposed in the literature to explain conductor-dielectric and dielectric-dielectric charge transfers driven by electric fields. In this model, the transferred carriers would be OH^- and H^+ ions, and strong experimental evidence supporting it has been reported.[36,37,39,40] Indeed, such mechanism could certainly account for the similarities between metallic and dielectric particles found in this work, as well as the essentially invariant behavior regardless of the sign of the PV charge. Relatedly, several studies have already analyzed the adsorption of water on LN surfaces[41–43] and other ferroelectrics.[44,45] Although we cannot fully disregard an electron transfer yet, an ion-dominated transfer appears more easily reconcilable with our experimental configuration and results. Lastly, the presence of micro/nano-discharges, perhaps promoted by the electrostatic field enhancement in the vicinity of the particles, could be another plausible mechanism.[46–49] The ions generated during the dielectric breakdown of the surrounding medium could mediate the transfer creating a conductive pathway. Anyhow, the coexistence of several mechanisms cannot be ruled out either, and further work is required to test these hypotheses and unravel the nature of this complex effect. As an additional step in that direction, we aimed to confirm whether illumination is necessary to induce charge transfer or the generation of charges with the corresponding fields at the ferroelectric surface is sufficient (whatever their origin). For that purpose, we addressed experiments in the dark exploiting instead the PY effect.

4. Thermally-Induced Charge Transfer by the Pyroelectric Effect

Since the generation of PV and PY fields relies on completely different mechanisms (light excitation vs temperature variation), PY experiments can offer valuable complementary information in the context of charge transfer and particle ejection. The procedure was similar to that of Section 2.4. First, a uniform background of particles was deposited on the ferroelectric surface (surrounded by air), and then, the temperature of the crystal was modified by a Peltier device (see the full setup in the Experimental Section). The temperature variation induces a change in the spontaneous polarization of the ferroelectric, thereby generating an imbalance between the polarization charges and the screening charges at the surface. In our case (LN and LT), the spontaneous polarization decreases or increases depending on whether the crystal is heated up or cooled down, respectively. In turn, this process gives rise to surface charges at the polar faces and, hence, an electric field (see **Figure 7**a).

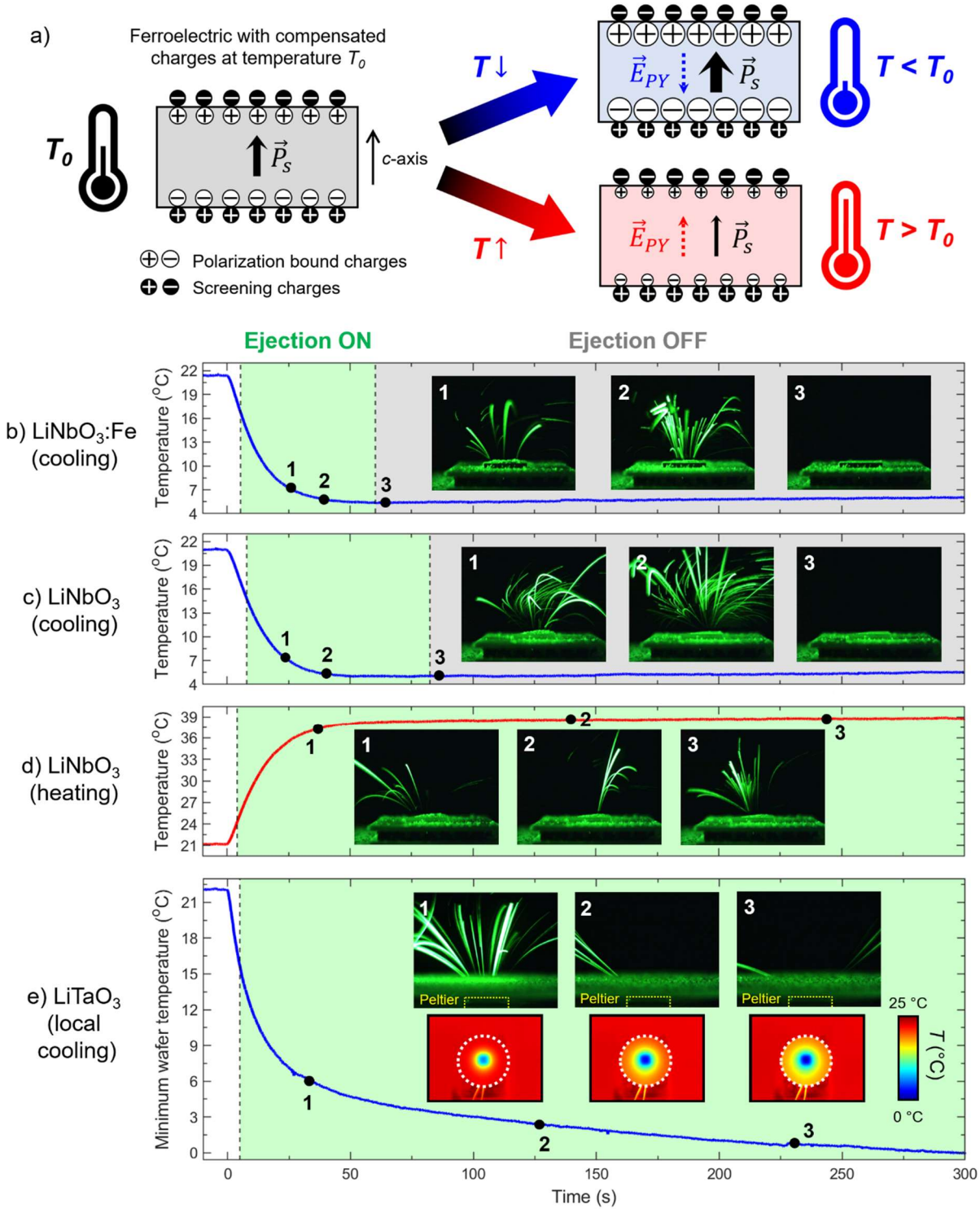

Figure 7. a) Illustration of the working principle behind the PY effect. The usual case of a material with a negative PY coefficient (like LN and LT) has been assumed in the representation, where the spontaneous polarization $\boldsymbol{P_s}$ decreases with increasing temperature. In figures b)-e) the experimental results of $CaCO_3$ particle ejection from *z*-cut LN:Fe (+*c* face), LN (+*c* face) and LT (–*c* face) are presented, with air as surrounding medium. The time evolution of the temperature has been plotted, along with lateral images at specific times indicated in the graphs. Note that the curve in e) corresponds to the minimum temperature of the LT wafer, since the temperature spatial distribution is inhomogeneous as shown in the thermograms (the white dotted circle indicates the edge of the wafer).

The experiments were carried out with *z*-cut samples and $CaCO_3$ particles. First, LN:Fe and undoped LN crystals were used (see Figure 7b-d and Video S3-S4). In these cases the surface temperature was observed to be uniform because the area of the Peltier cell was much larger than that of the samples. The time evolution of the temperature is plotted in Figure 7b-d for each experiment, along with selected illustrative images from the lateral camera. A few seconds after turning on the Peltier current we observed the onset of particle ejection, corresponding to temperature changes of around $|\Delta T| \approx$ 3-6 °C. At the beginning most particles were ejected from the edges of the crystal surface, which we attribute to the enhanced electric field at the plate edge. As the temperature kept decreasing/rising, more particles closer to the sample center were repelled away and the overall ejection rate progressively increased. The closer to the center, the lower the angle of the particle trajectories with respect to the surface normal, as dictated by the PY field distribution.[50] Eventually, as the number of particles on the surface dwindled, the ejection rate slowed down. At this point we noticed some differences between cooling and heating experiments. Upon cooling, the ejection activity fully stopped around 60-90 s after turning on the Peltier cell (see Figure 7b and 7c). Instead, when the samples were heated up, the ejection was slightly less efficient and it persisted for significantly longer times (see Figure 7d). The origin of this difference remains unclear. On the other hand, the behavior of iron-doped and undoped LN crystals was found to be similar, most likely due to the small impact of iron doping on the PY coefficient of LN.[51] For that reason, in Figure 7 we have omitted the heating experiment with LN:Fe, since it is analogous to undoped LN. Furthermore, both polar faces (+*c* and −*c*) qualitatively showed very similar performances as in the experiments with the bulk PV effect. Also, no ejection whatsoever was obtained in control experiments with passive glass substrates instead of LN, as expected.

Finally, we addressed the possibility of using other ferroelectrics to show the generality of this effect beyond LN. For that purpose, a full *z*-cut LT wafer with a diameter of 2" was employed.

At variance with the previous experiments, in this case we chose a Peltier module with an area (9×9 mm^2) much smaller than the LT wafer to locally cool it down. The results are illustrated in Figure 7e, where the minimum temperature of the wafer has been plotted as a function of time, along with selected pictures and thermal maps at those instants. Indeed, thermally-driven ejection was generated with LT analogously to LN, starting shortly after switching on the Peltier cell. A fragment of the ejection footage may be found in Video S5. However, in contrast to Figure 7b-c, here the ejection never fully stopped (in our timescale) owing to the slower temperature evolution and lateral heat conduction. For the latter reason, the boundaries of the ejection-active region spread away from the center over time. By the end of the experiment, a very clear particle deficit had been generated at the center of the wafer, coinciding with the position of the Peltier cell as expected.

Considering that the ejection results obtained with both the PV and PY effects in air are rather similar, it is reasonable to propose that the underlying physical mechanism here is also a charge transfer (depicted in Figure 6a for the bulk PV effect). Upon thermal stimuli (either cooling or heating), a charge transfer takes place between the PY substrate and the particles in contact with it, leading to their repulsion. More specifically, particles get negatively charged at the +*c* face upon heating or at the –*c* face upon cooling, whereas they get positively charged at the +*c* face upon cooling or at the –*c* face upon heating. The heating/cooling degree of freedom allows us to tune the sign of the transferred charge on a ferroelectric surface with a given polarity, which is not possible with the bulk PV effect alone. The fact that this charge transfer can be induced by temperature variations hints that light excitation is not a cornerstone of the underlying mechanism, but only one possible pathway to drive it via the bulk PV effect. Likewise, the need for a minimum temperature change suggests the existence of a certain threshold for ejection to occur. Nonetheless, the results of Figure 7 show that such variations are very moderate and easily attainable. In fact, the effect can be triggered by mere contact with the human body (see

Video S6). Lastly, the PY spatial control may be improved by using focused IR light sources at suitable wavelengths,[5,50,52] hot tips[5] or micro-heaters[53] to locally heat up the crystals, although the bulk PV effect is far superior in terms of spatial resolution.

5. Conclusions and Outlook

A novel phenomenon observed in the hybrid system composed of a ferroelectric crystal and micro/nanoparticles on its surface is systematically investigated, providing a comprehensive set of experimental data and a thorough analysis. The phenomenon consists in a charge transfer between the ferroelectric and the particles, activated by illumination or temperature changes, leading to particle repulsion/ejection from the ferroelectric surface. The generality of the phenomenon is shown since it is observed regardless of the nature of the particles, metallic (Ag and Al) or dielectric ($CaCO_3$ and Al_2O_3), and in different surrounding media (heptane, air). By probing the charge state of the particles after ejection, we have clearly demonstrated that they acquire a net negative/positive charge at $+c/-c$ ferroelectric surfaces (i.e. same sign as the PV charge). This remarkable result satisfactorily accounts for the repulsive ejection behavior. Additional evidence gathered with *x*-cut crystals, mainly particle trajectories and spatial distribution of ejection-active regions, further supports the charge transfer mechanism.

Although most experiments are developed under light activation, we have also proved that the ejection of particles can also be induced thermally, both upon cooling and heating, assisted by the PY effect readily available in any ferroelectric. The phenomenon has been successfully observed in a variety of materials, namely LN:Fe, LN and LT samples, showing the generality of the effect that is indeed not specific to LN. Furthermore, the PY results shed new light on the underlying particle charging mechanism, as these experiments do not involve optical excitation, indicating that the key ingredient of the charge transfer mechanism is the presence of space charge distributions and the corresponding electric fields at the surface. In this context, we believe that particle ejection by mechanical stress could also be achieved thanks to the

piezoelectric effect, not studied in this paper. Similarly, the effect could plausibly be extended to non-ferroelectric pyroelectrics and piezoelectrics.

From a practical point of view, the fact that the effect is activated and controlled by low/moderate light intensities (PV) or temperature variations (PY), without any electrodes or high-voltage power supplies, is rather appealing. In that sense, a variety of applications are envisioned. First, it allows erasure and reconfiguration of particle patterns and structures assembled on ferroelectric platforms.[19] In addition, it could be used as a low-cost simple method to generate suspensions of charged particles, with control over the charge sign and possibly reduced aggregation (without functionalization). In the context of PVOT or other electrostatic manipulation techniques, such suspensions would be useful to operate via electrophoretic forces (repulsive or attractive). Other functions could be locally transferring particles to nearby surfaces, contactless cleaning surfaces or propelling micro/nano-particles. Also, the high spatial resolution offered by the bulk PV effect could potentially allow charge transfer processes with sub-micron optical control.

6. Experimental Section

Ferroelectric Materials and Particles. For the experiments based on the bulk PV effect, *z*-cut and *x*-cut LN:Fe crystals were used, with 0.25 mol% iron doping level and thickness of 1 mm. Aside from LN:Fe samples, other ferroelectrics were explored in Section 4, devoted to the PY effect. In particular, undoped *z*-cut LN and LT crystals were selected, both having a thickness of 1 mm. The direction of the polar *c*-axis was characterized using the PY method explained in ref. [54]: the crystals were heated up and the sign of the voltage generated between the polar faces was observed. On the other hand, four different types of particles were used throughout this work: Ag nanoparticles (average diameter d = 100 nm, purchased from SkySpring Nanomaterials), Al nanoparticles (d = 70 nm, SkySpring Nanomaterials), Al_2O_3 microparticles (d = 1 μm) and $CaCO_3$ microparticles (handmade by crushing chalk, typical size d = 1-10 μm,

irregular shape). All these particles were preserved in powder form and dispersed in *n*-heptane (nonpolar liquid) by sonication when necessary (with particle concentrations ranging between 50 mg L^{-1} and 300 mg L^{-1}).

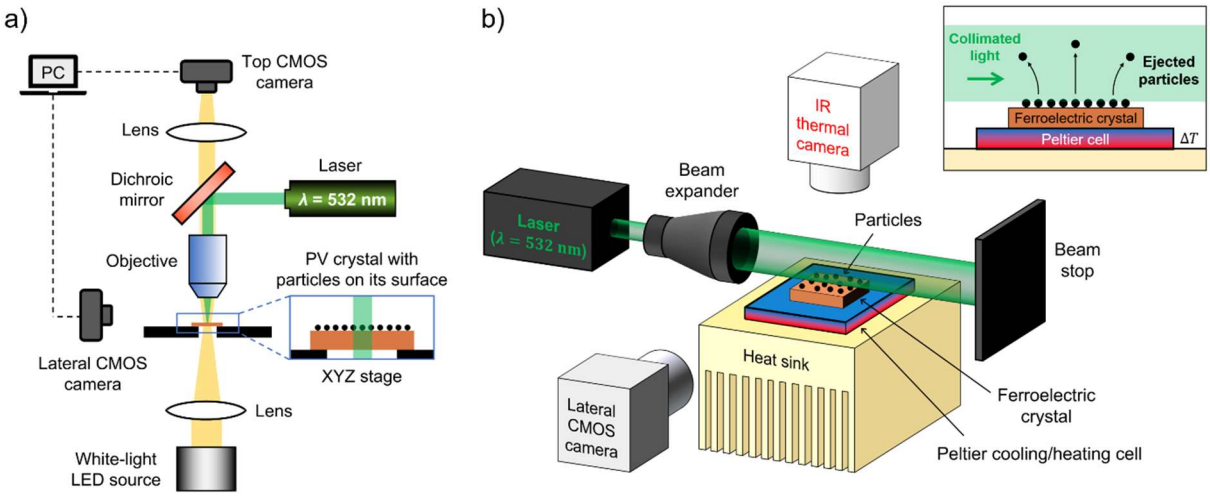

Figure 8. Experimental setups employed to study a) light-induced particle ejection from the surface of PV ferroelectric crystals, and b) thermally-induced particle ejection from the surface of ferroelectric crystals through the PY effect. The inset at the top right corner of b) shows the lateral view as seen from the perspective of the lateral CMOS camera.

Experimental Setups. Two different setups were mainly used to investigate the phenomenon of particle ejection from the surface of ferroelectric materials. They are schematically illustrated in **Figure 8**. The experimental system of Figure 8a was devoted to monitor the ejection produced by light excitation due to the bulk PV effect. This setup allows for illumination of a PV crystal by a Gaussian laser beam, as well as real-time visualization of the particle dynamics above the surface of the crystal. Two different situations may be distinguished depending on whether the particles are immersed in a liquid or surrounded by air. In the first case, the PV substrate was placed inside a cuvette filled with suspension. After a few minutes of sedimentation, some particles form a homogeneous background on the substrate surface while others may remain suspended. Then, the crystal was illuminated. The excitation laser beam was focused by an objective lens (20X, numerical aperture NA = 0.42), obtaining a $1/e^2$ spot diameter of $2w$ = 150 ± 20 μm at the crystal surface (measured with a beam profiler, NS2-

SI/9/5-PRO Ophir Optronics). It is worth noting that the object plane of our optical system does not coincide with the focal plane of the objective. Thus, the spot size does not correspond to the beam waist. The behavior of the particles on the surface was simultaneously recorded in real time by means of the top CMOS camera (DFK MKU130-10x22, The Imaging Source). The intensity of the white-light LED used for observation purposes was maintained lower than 80 $\mu W\ cm^{-2}$ to guarantee a negligible PV contribution in our timescales. For the experiments in air, the objective lens of Figure 8a was removed, hence working with an unfocused beam diameter of $2w$ = 3 mm. Besides, a lateral CMOS camera was added to observe particle trajectories above the crystal surface (DCC1645C-HQ, Thorlabs). The laser scattering produced by the particles was enough to track their paths without any other light source. It is worth noting that, in all our experiments based on optical excitation, the pyroelectric contribution was fully negligible compared to the bulk photovoltaic effect. Measurements made by an IR thermal camera revealed that the temperature increase due to light absorption was $\lesssim$ 1 °C in air (using the intensities, spot sizes and samples of this work).

On the other hand, the setup of Figure 8b was designed to study particle ejection induced by temperature variations of the ferroelectric crystals. For that purpose, Peltier thermoelectric modules (from Supercool) were used to flexibly cool down or heat up the samples, driven by a commercial controller (TED350, Thorlabs) operating in constant-current mode. Moreover, the Peltier cells were placed on top of a computer heat sink applying thermal paste (Tacens MT1) to ensure a good thermal contact between them. To track the temperature of the upper ferroelectric surface during the experiments, a thermal camera was placed above the crystals as shown in Figure 8b (VarioCAM HDx head 675, InfraTec GmbH, working in the 7.5-14 µm IR range), tilted by a small angle of 15° with respect to the crystal surface normal. In those conditions, the thermal emissivity of the crystals was calibrated using the typical black tape method (see Supporting Information). To observe particle trajectories, the area right above the

sample was laterally illuminated by an expanded collimated beam, as illustrated in the inset of Figure 8b. This arrangement allowed us to fully suppress any possible PV contribution. The paths of the ejected particles were traced via light scattering by using the same lateral CMOS camera as in Figure 8a.

Supporting Information
Supporting Information is available from the Wiley Online Library or from the author.

Acknowledgements

Financial support from the Ministerio de Ciencia, Innovación y Universidades (MICIU) of Spain (project number MAT2017- 83951-R) is gratefully acknowledged. C. S-V acknowledges support from the MICIU through his FPU contract (ref. FPU19/03940). We also thank Dr. José Luis Plaza (Universidad Autónoma de Madrid) for supplying the Al_2O_3 particles.

Received: ((will be filled in by the editorial staff))
Revised: ((will be filled in by the editorial staff))
Published online: ((will be filled in by the editorial staff))

References

[1] A. Blázquez-Castro, A. García-Cabañes, M. Carrascosa, *Appl. Phys. Rev.* **2018***, 5*, 041101.

[2] W. Wang, J. Li, H. Liu, S. Ge, *Adv. Sci.* **2021**, *8*, 2003074.

[3] S. V. Kalinin, D. A. Bonnell, T. Alvarez, X. Lei, Z. Hu, R. Shao, J. H. Ferris, *Adv. Mater.* **2004**, *16*, 795.

[4] J. F. Scott, *Science* **2007**, *315*, 954.

[5] P. Ferraro, S. Coppola, S. Grilli, M. Paturzo, V. Vespini, *Nat. Nanotechnol.* **2010**, *5*, 429.

[6] L. Liang, X. Kang, Y. Sang, H. Liu, *Adv. Sci.* **2016**, *3*, 1500358.

[7] M. O. Ramírez, P. Molina, A. Gómez-Tornero, D. Hernández-Pinilla, L. Sánchez-García, S. Carretero-Palacios, L. E. Bausá, *Adv. Mater.* **2019**, *31*, 1901428.

[8] H. Guan, J. Hong, X. Wang, J. Ming, Z. Zhang, A. Liang, X. Han, J. Dong, W. Qiu, Z. Chen, H. Lu, H. Zhang, *Adv. Opt. Mater.* **2021**, 2100245.

[9] H. A. Eggert, F. Y. Kuhnert, K. Buse, J. R. Adleman, D. Psaltis, *Appl. Phys. Lett.* **2007**, *90*, 241909.

[10] S. Grilli, P. Ferraro, *Appl. Phys. Lett.* **2008**, *92*, 232902.

[11] X. Zhang, J. Wang, B. Tang, X. Tan, R. A. Rupp, L. Pan, Y. Kong, Q. Sun, J. Xu, *Opt. Express* **2009**, *17*, 9981.

[12] M. Carrascosa, A. García-Cabañes, M. Jubera, J. B. Ramiro, F. Agulló-López, *Appl. Phys. Rev.* **2015**, *2*, 040605.

[13] I. Elvira, J. F. Muñoz-Martínez, M. Jubera, A. García-Cabañes, J. L. Bella, P. Haro-González, M. A. Díaz-García, F. Agulló-López, M. Carrascosa, *Adv. Mater. Technol.* **2017**, *2*, 1700024.

[14] R. Rega, J. F. Muñoz-Martínez, V. Pagliarulo, A. Longo, M. Palomba, G. Carotenuto, P. Ferraro, S. Grilli, *Adv. Mater. Interfaces* **2021**, *8*, 2002216.

[15] J. Villarroel, H. Burgos, Á. García-Cabañes, M. Carrascosa, A. Blázquez-Castro, F. Agulló-López, *Opt. Express* **2011**, *19*, 24320.

[16] A. García-Cabañes, A. Blázquez-Castro, L. Arizmendi, F. Agulló-López, M. Carrascosa, *Crystals* **2018**, *8*, 65.

[17] S. Grilli, S. Coppola, G. Nasti, V. Vespini, G. Gentile, V. Ambrogi, C. Carfagna, P. Ferraro, *RSC Adv.* **2014**, *4*, 2851.

[18] A. Gallego, A. García-Cabañes, M. Carrascosa, L. Arizmendi, *J. Phys. Chem. C* **2016**, 120, 731.

[19] C. Sebastián-Vicente, E. Muñoz-Cortés, A. García-Cabañes, F. Agulló-López, M. Carrascosa, *Part. Part. Syst. Charact.* **2019**, *36*, 1900233.

[20] A. M. Glass, D. von der Linde, T. J. Negran, *Appl. Phys. Lett.* **1974**, *25*, 233.

[21] B. Sturman, V. Fridkin, *Photovoltaic and Photorefractive Effects in Noncentrosymmetric Materials*, Gordon and Breach Science Publishers, Philadelphia **1992**.

[22] E. M. de Miguel-Sanz, J. Limares, M. Carrascosa, L. Arizmendi, *J. Opt. Soc. Am. B* **2000**, *17*, 1140.

[23] F. Agulló-López, G. F. Calvo, M. Carrascosa, in *Photorefractive Materials and Their Applications 1* (Eds: P. Günter, J. P. Huignard), Springer, New York, USA **2006**, Ch. 3.

[24] M. Esseling, A. Zaltron, C. Sada, C. Denz, *Appl. Phys. Lett.* **2013**, *103*, 061115.

[25] J. F. Muñoz-Martínez, I. Elvira, M. Jubera, A. García-Cabañes, J. B. Ramiro, C. Arregui, M. Carrascosa, *Opt. Mat. Express* **2015**, *5*, 1137.

[26] T. B. Jones, *Electromechanics of particles*, Cambridge University Press, Cambridge, UK **1995**.

[27] J. F. Muñoz-Martínez, J. B. Ramiro, A. Alcázar, A. García-Cabañes, M. Carrascosa, *Phys. Rev. Appl.* **2017**, *7*, 064027.

[28] C. Arregui, J. B. Ramiro, A. Alcázar, A. Méndez, H. Burgos, A. García-Cabañes, M. Carrascosa, *Opt. Express* **2014**, *22*, 29099.

[29] J.F. Muñoz-Martínez, A. Alcázar, M. Carrascosa, *Opt. Express* **2020**, *28*, 18085.

[30] A. Y. H. Cho, *J. Appl. Phys.* **1964**, *35*, 2561.

[31] G. M. Colver, *J. Appl. Phys.* **1976**, *47*, 4839.

[32] T. Pähtz, H. J. Herrmann, T. Shinbrot, *Nat. Phys.* **2010**, *6*, 364.

[33] K. J. M. Bishop, A. M. Drews, C. A. Cartier, S. Pandey, Y. Dou, *Langmuir* **2018**, *34*, 6315.

[34] M. Shoyama, S. Nishida, S. Matsusaka, *Adv. Powder Technol.* **2019**, *30*, 2052.

[35] L. Xie, Y. Liu, C. Zhou, M. Wang, D. J. Lacks, J. Zhou, *Aeolian Res.* **2021**, *50*, 100675.

[36] Y. Zhang, T. Pähtz, Y. Liu, X. Wang, R. Zhang, Y. Shen, R. Ji, B. Cai, *Phys. Rev. X* **2015**, *5*, 011002.

[37] A. Sayyah, M. Mirzadeh, Y. Jiang, W. V. Gleason, W. C. Rice, M. Z. Bazant, *Phys. Rev. Appl.* **2020**, *13*, 034071.

[38] L. S. McCarty, G. M. Whitesides, *Angew. Chem. Int. Ed. Engl.* **2008**, *47*, 2188.

[39] M. Sow, R. Widenor, A. R. Akande, K. S. Robinson, R. M. Sankaran, D. J. Lacks, *J. Braz. Chem. Soc.* **2013**, *24*, 273.

[40] V. Lee, N. M. James, S. R. Waitukaitis, H. M. Jaeger, *Phys. Rev. Mat.* **2018**, *2*, 035602.

[41] S. Sanna, W. G. Schmidt, *J. Phys.: Condens. Matter* **2017**, *29*, 413001.

[42] K. Cordero-Edwards, L. Rodríguez, A. Calò, M. J. Esplandiu, V. Pérez-Dieste, C. Escudero, N. Domingo, A. Verdaguer, *J. Phys. Chem. C* **2016**, *120*, 24048.

[43] C. Yue, X. Lu, J. Zhang, F. Huang, J. Zhu, *Phys. Rev. B* **2019**, *100*, 245432.

[44] X. Li, B. Wang, T. Y. Zhang, Y. Su, *J. Phys. Chem. C* **2014**, *118*, 15910.

[45] N. Domingo, I. Gaponenko, K. Cordero-Edwuards, N. Stucki, V. Pérez-Dieste, C. Escudero, E. Pach, A. Verdaguer, P. Patrycja, *Nanoscale* **2019**, *11*, 17920.

[46] A. T. Pérez, *J. Electrostat.* **2002**, *56*, 199.

[47] G. Eslami, E. Esmaeilzadeh, A. T. Pérez, *Phys. Fluids* **2016**, *28*, 107102.

[48] E. S. Elton, E. R. Rosenberg, W. D. Ristenpart, *Phys. Rev. Lett.* **2017**, *119*, 094502.

[49] C. Pan, J. Tang, G. Chen, Y. Zhang, X. Luo, *High Volt.* **2020**, *5*, 287.

[50] W. Yan, C. Zhao, W. Luo, W. Zhang, X. Li, D. Liu, *ACS Appl. Mater. Interfaces* **2021**, *13*, 23181.

[51] T. Bartholomäus, K. Buse, C. Deuper, E. Krätzig, *Phys. Status Solidi A* **1994**, *142*, K55.

[52] W. Li, X. Tang, L. Wang, *Sci. Adv.* **2020**, *6*, eabc1693.

[53] G. Nasti, S. Coppola, V. Vespini, S. Grilli, A. Vettoliere, C. Granata, P. Ferraro, *Adv. Intell. Syst.* **2020**, *2*, 2000044.

[54] R. S. Weis, T. K. Gaylord, *Appl. Phys. A* **1985**, *37*, 191.

A. García-Cabañes, F. Agulló-López, M. Carrascosa*

Light and Thermally-Induced Charge Transfer and Ejection of Micro/Nanoparticles from Ferroelectric Crystal Surfaces

ToC figure

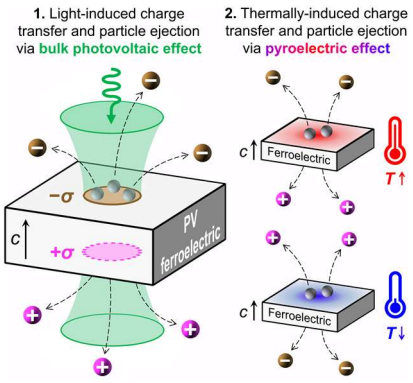

A novel phenomenon in the hybrid interacting system formed by ferroelectrics and micro/nanoparticles located on their surface is reported. Visible illumination or temperature variations trigger a contact charge transfer between the ferroelectrics and the particles, leading to electrostatic repulsion and particle ejection. The phenomenon provides additional functionalities to ferroelectric platforms for multiple applications, such as micro/nanoparticle manipulation or nanoparticle charging.

Supporting Information

Light and Thermally-Induced Charge Transfer and Ejection of Micro/Nanoparticles from Ferroelectric Crystal Surfaces

*Carlos Sebastián-Vicente, Angel García-Cabañes, Fernando Agulló-López, and Mercedes Carrascosa**

Supporting Figures

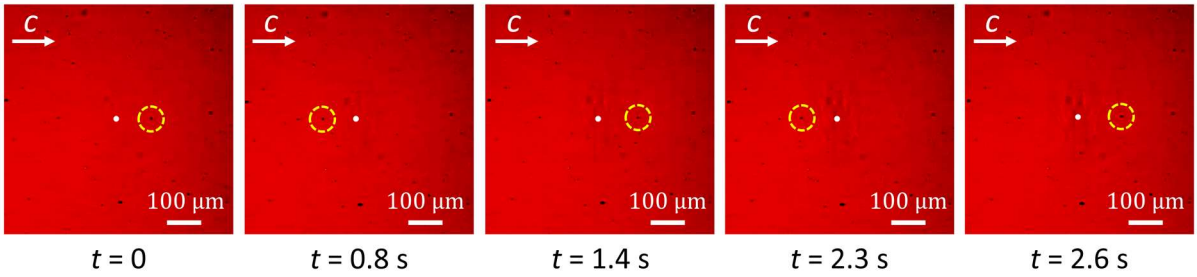

Figure S1. Sequence of images showing an example of several consecutive oscillations made by a specific aggregate of Ag nanoparticles on an *x*-cut LN:Fe substrate illuminated by a Gaussian beam ($2w$ = 150 µm, I = 6.1 W cm^{-2}). The white dot in the middle of the images indicates the center of the static light beam, whereas the position of the particle aggregate is highlighted by a yellow circle. After switching on the illumination at t = 0, the aggregate starts oscillating between the $+c$ and the $-c$ sides of the light spot.

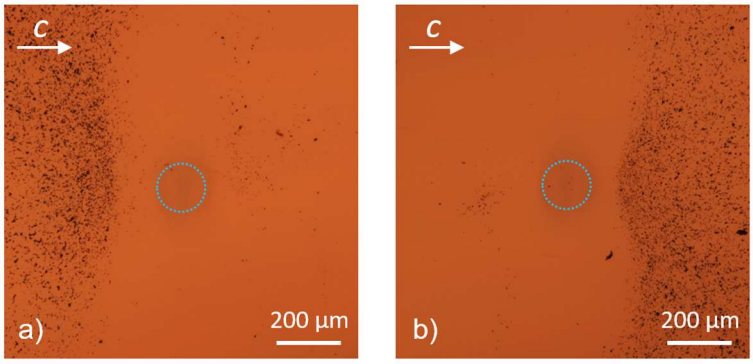

Figure S2. Charge tests for dielectric $CaCO_3$ particles ejected from a) the $+c$ face and b) the $-c$ face of a *z*-cut crystal. The experimental configuration, procedure and illumination parameters are identical to those of Figure 6.

Supporting Videos

Video S1. PV-driven ejection of $CaCO_3$ particles in air from a *z*-cut LN:Fe crystal under illumination. Beam diameter $2w = 3$ mm, intensity 86 mW cm^{-2}.

Video S2. PV-driven ejection of $CaCO_3$ particles in air from an *x*-cut LN:Fe crystal under illumination. Beam diameter $2w = 3$ mm, intensity 86 mW cm^{-2}.

Video S3. Fragment of the PY experiment corresponding to Figure 7c, illustrating the ejection of $CaCO_3$ particles in air from a *z*-cut LN crystal upon cooling.

Video S4. Fragment of the PY experiment corresponding to Figure 7d, illustrating the ejection of $CaCO_3$ particles in air from a *z*-cut LN crystal upon heating.

Video S5. Fragment of the PY experiment corresponding to Figure 7e, illustrating the ejection of $CaCO_3$ particles in air from a *z*-cut LT wafer upon local cooling (using a Peltier cell significantly smaller than the wafer, as described in Section 4 and indicated in the video).

Video S6. PY-driven ejection of $CaCO_3$ particles in air from a *z*-cut LN crystal in contact with a forearm. Room temperature was around 25 ºC and forearm skin temperature was around 33.5 ºC.

Determination of the Thermal Emissivity

An essential parameter when using IR cameras to measure temperature is the thermal emissivity of the target. In this case, we were interested in the emissivity of the ferroelectric crystals employed in PY experiments (namely LN, LN:Fe and LT), and we employed the widespread black tape method to determine it, using 3M Scotch Super 33+ black electrical tape as a reference.[1,2] The emissivity of this particular tape in the IR range of our camera is approximately $\varepsilon = 0.96$, and an uncertainty of ± 0.01 was assumed for this value. On the other hand, the so-called reflected apparent temperature was measured using a piece of highly reflective aluminum foil.[2] All measurements were performed with the IR camera forming an angle of around 15° with respect to the normal of the surface under analysis. Also, care was taken to avoid undesired thermal reflections.

A piece of tape was attached to the surface of the crystals, so that one can assure that they are at the same temperature. The emissivity of the camera software was set to $\varepsilon = 1$. Then, a Peltier

cell was used to change their temperature. From the temperature readings of the attached tape and the bare crystal surfaces, the emissivity could be computed as:[1]

$$\varepsilon_c = \varepsilon_t \cdot \frac{\tilde{T}_c^4 - T_0^4}{\tilde{T}_t^4 - T_0^4} \tag{S1}$$

where $\tilde{T}_c$ and $\tilde{T}_t$ are the temperature readings of the crystal and the tape (note that the readings for $\varepsilon = 1$ do not correspond to the actual target temperature), T_0 is the reflected apparent temperature, ε_t the emissivity of the tape and ε_c the emissivity of the crystal. The emissivity was measured below and above room temperature (near 0 °C up to 60 °C), covering the working range of this work. Measurements near 0 °C were carried out on low-humidity days to avoid the influence of water condensation on surfaces below the dew point. We obtained the same value below and above room temperature: $\varepsilon_c = 0.79 \pm 0.02$ for LN (undoped and iron-doped) and $\varepsilon_c = 0.82 \pm 0.02$ for LT (undoped).

Temperature Measurements During PY-based Ejection Experiments

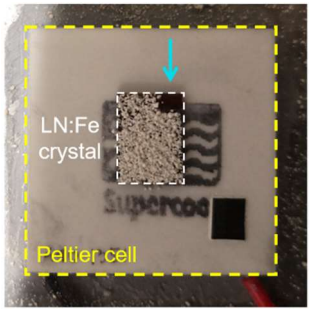

Figure S3. Photograph of a LN:Fe crystal with a background of $CaCO_3$ particles on its surface for a PY experiment. The blue arrow indicates the top right corner of the sample, free of particles to measure its temperature.

The thermal emissivity of the crystals was used to correct the temperature readings of the IR camera, along with the reflected apparent temperature (determined for each experiment). To avoid minor disturbances of the temperature measurements caused by the $CaCO_3$ particles, no particles were deposited on one of the corners in experiments with small samples of LN:Fe and LN (see Figure S3). In those cases, the surface temperature was homogeneous across the crystal

area (because the Peltier cell was significantly larger than the crystals, as shown in Figure S3), and so, the surface temperature could be reliably measured at the corner. In contrast, this approach was not applicable to the experiment with the LT wafer (see Figure 7e), as the temperature distribution was inhomogeneous. However, due to the space gaps between particles and the spatial resolution of the thermograms, the minimum temperature of the wafer plotted in Figure 7e could be extracted with very little error. Specifically, the IR camera has a 640×480 pixel resolution, so that each pixel covers an area of about 180×180 μm^2 in the thermograms of Figure 7e. Besides, from those thermograms it is clear that the spatial information is barely affected by the presence of the particles.

References Supporting Information

[1] R. P. Madding, *Proc. SPIE* **1999**, *3700*, 393.

[2] R. Usamentiaga, P. Venegas, J. Guerediaga, L. Vega, J. Molleda, F. G. Bulnes, *Sensors* **2014**, *14*, 12305.